

Progressive Contrast Registration for High-Fidelity Bidirectional Photoacoustic Microscopy Alignment

Jiahao Qin*

Email: jiahao.qin19@gmail.com

Abstract. High-speed optical-resolution photoacoustic microscopy (OR-PAM) with bidirectional raster scanning doubles imaging speed but introduces coupled domain shift and geometric misalignment between forward and backward scan lines. Existing methods, constrained by brightness constancy assumptions, achieve limited alignment quality ($\text{NCC} \leq 0.96$). We propose PCReg-Net, a progressive contrast-guided registration framework that performs coarse-to-fine alignment through four lightweight modules: (1) a registration U-Net for coarse alignment, (2) a reference feature extractor capturing multi-scale structural cues, (3) a contrast module that identifies residual misalignment by comparing coarse-registered and reference features, and (4) a refinement U-Net with feature injection for high-fidelity output. We further propose the Temporal NCC (TNCC) and Temporal NCC Gap (TNCG) for reference-free evaluation of inter-frame temporal consistency. On OR-PAM-Reg-4K (432 test samples), PCReg-Net achieves NCC of 0.983, SSIM of 0.982, and PSNR of 46.96 dB, surpassing the state-of-the-art by over 14 dB at real-time speed. Code is available at <https://github.com/JiahaoQin/PCReg-Net>.

Keywords: Photoacoustic microscopy · Image registration · Progressive refinement · Contrast learning

1 Introduction

Optical-resolution photoacoustic microscopy (OR-PAM) combines the cellular-level spatial resolution of optical imaging with the sensitivity of photoacoustic detection, enabling label-free visualization of endogenous chromophores such as hemoglobin, melanin, and lipids [18, 21, 22]. High-speed OR-PAM systems employ bidirectional raster scanning [20, 6] to nearly double the imaging frame rate, facilitating the capture of rapid hemodynamic events in *in vivo* cerebral microvasculature [19, 5].

However, bidirectional scanning introduces systematic artifacts that severely compromise image quality. Forward and backward scan lines exhibit coupled domain shift and geometric misalignment arising from mechanical hysteresis, velocity asymmetry, and scan-direction-dependent system response [16, 9]. These

* Corresponding author.

artifacts manifest as spatial offsets between adjacent columns and intensity differences that violate the brightness constancy assumption underlying conventional registration methods [4].

Existing approaches to this problem fall into two categories. Classical registration methods, including SIFT [8], Demons [17], optical flow [7], and SyN [1], attempt direct spatial alignment but achieve limited accuracy ($\text{NCC} \leq 0.72$) because they cannot compensate for intensity differences between forward and backward acquisitions. Recent deep learning methods such as VoxelMorph [2] and TransMorph [3] learn to predict deformation fields but similarly assume comparable intensity distributions, yielding suboptimal results under domain shift. Multimodal alignment strategies [15] can mitigate modality gaps yet remain under-explored for microscopy registration. Domain-invariant registration [14] and scene-appearance separation frameworks [10] address domain shift through disentangled representations, with the latter achieving NCC of 0.96, but the complex generative architecture with separate content and style pathways limits the reconstruction fidelity achievable in the pixel space.

We observe that the key limitation of prior methods is the indirect treatment of alignment: deformation-based approaches warp pixel intensities without accounting for domain shift, while generative approaches address domain shift but introduce reconstruction noise that limits fine-grained alignment. Although cross-modal representation learning [11] has shown promise in bridging heterogeneous feature spaces, aligning microscopy scan lines demands pixel-level fidelity beyond what latent-space methods provide. In contrast, a direct image-to-image registration paradigm that progressively refines the alignment through explicit comparison with the reference image can circumvent both limitations.

In this paper, we propose PCReg-Net, a progressive contrast-guided registration framework for high-fidelity bidirectional OR-PAM alignment. The core idea is to decompose the registration into two stages: a coarse alignment that approximates the target, followed by a contrast-guided refinement that identifies and corrects residual discrepancies by explicitly comparing coarse-registered features with reference features at multiple scales. The main contributions are:

1. We propose PCReg-Net, a progressive coarse-to-fine registration framework consisting of four lightweight modules that achieves high-fidelity alignment ($\text{NCC} = 0.983$) by separating coarse registration from contrast-guided refinement.
2. We introduce a multi-scale contrast module that generates residual alignment cues by comparing features from the coarse-registered and reference images, along with a feature injection mechanism that guides the refinement network using these contrast signals.
3. We conduct comprehensive evaluation on two OR-PAM benchmarks, demonstrating over 14 dB PSNR improvement over the state-of-the-art. We further propose two novel temporal evaluation metrics—Temporal NCC (TNCC) and Temporal NCC Gap (TNCG)—for reference-free assessment of inter-frame consistency, and show that PCReg-Net preserves natural temporal coherence with near-zero TNCG.

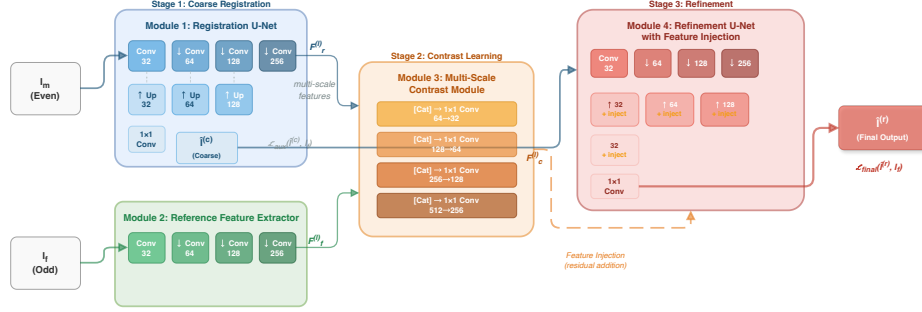


Fig. 1. Overview of the progressive contrast registration framework. The moving image I_m is first coarsely aligned by the Registration U-Net, producing $\hat{I}^{(c)}$ and multi-scale features. A Reference Feature Extractor captures structural cues from the fixed image I_f . The Multi-Scale Contrast Module compares features at four scales (32, 64, 128, 256 channels), generating contrast signals that highlight residual misalignment. The Refinement U-Net with feature injection produces the final registered output $\hat{I}^{(r)}$.

2 Method

2.1 Overview

The proposed progressive contrast registration framework takes as input a pair of column images: the moving image I_m (even/backward scan columns) and the fixed image I_f (odd/forward scan columns), both of size $H \times W$. The goal is to produce a registered output $\hat{I}^{(r)}$ that is aligned with I_f in both geometry and intensity.

As illustrated in fig. 1, the framework consists of four modules:

1. **Registration U-Net \mathcal{R} :** Produces the coarse registration $\hat{I}^{(c)} = \mathcal{R}(I_m)$ and extracts multi-scale features $\{F_r^{(l)}\}_{l=1}^4$.
2. **Reference Feature Extractor \mathcal{E} :** Extracts multi-scale features $\{F_f^{(l)}\}_{l=1}^4$ from the fixed image I_f .
3. **Multi-Scale Contrast Module \mathcal{C} :** Compares registration and reference features at each scale to produce contrast features $\{F_c^{(l)}\}_{l=1}^4$.
4. **Refinement U-Net \mathcal{U} :** Takes the coarse registration $\hat{I}^{(c)}$ and contrast features to produce the final output: $\hat{I}^{(r)} = \mathcal{U}(\hat{I}^{(c)}, \{F_c^{(l)}\})$.

2.2 Registration U-Net

The Registration U-Net performs initial coarse alignment using a lightweight encoder-decoder architecture. To minimize cost, each resolution level uses a single convolution block ($\text{Conv}_{3 \times 3}$ -BN-ReLU) rather than the double-convolution design in standard U-Net. The encoder downsamples via max pooling through

four levels with channels $C_l \in \{32, 64, 128, 256\}$, while the decoder upsamples via bilinear interpolation and concatenates skip-connected encoder features, followed by a single convolution block. A final 1×1 convolution maps the 32-channel output to single-channel image space. The network produces two outputs: the coarse-registered image $\hat{I}^{(c)} = \mathcal{R}(I_m)$ and multi-scale encoder features $\{F_r^{(l)}\}_{l=1}^4$, which are passed to the contrast module.

2.3 Reference Feature Extraction

A separate encoder-only network extracts multi-scale features $\{F_f^{(l)}\}_{l=1}^4$ from the fixed image I_f . It follows the same $32 \rightarrow 64 \rightarrow 128 \rightarrow 256$ channel progression with identical single-convolution blocks to ensure feature-space compatibility with the registration encoder. The weights are *not* shared with the Registration U-Net, allowing each encoder to specialize: the registration encoder learns transformation-relevant features from the moving image, while the reference encoder captures the structural content of the target.

2.4 Multi-Scale Contrast Module

The multi-scale contrast module is the core component that bridges coarse and fine registration. At each scale l , registration features $F_r^{(l)}$ and reference features $F_f^{(l)}$ are concatenated along the channel dimension and processed through a 1×1 convolution followed by batch normalization and ReLU activation:

$$F_c^{(l)} = \text{ReLU} \left(\text{BN} \left(\text{Conv}_{1 \times 1} \left([F_f^{(l)}; F_r^{(l)}] \right) \right) \right), \quad (1)$$

where $[\cdot; \cdot]$ denotes channel-wise concatenation and $\text{Conv}_{1 \times 1}$ reduces the $2C_l$ -channel input back to C_l channels. This design enables the contrast features to encode the difference between the current registration state and the target, providing explicit guidance for the refinement stage. The 1×1 convolution learns to identify misalignment patterns across corresponding feature channels without imposing spatial smoothness constraints, preserving fine-grained residual information.

2.5 Refinement U-Net with Feature Injection

The Refinement U-Net takes the channel-wise concatenation of $\hat{I}^{(c)}$ and the finest-scale contrast feature $F_c^{(1)}$ as input ($1 + 32 = 33$ channels), processed through the same lightweight encoder structure. The key innovation is the *feature injection* mechanism: at each of the four decoder levels, the decoded features are augmented with projected contrast features via residual addition:

$$\hat{X}^{(l)} = X^{(l)} + W^{(l)} \tilde{F}_c^{(l)}, \quad (2)$$

where $X^{(l)}$ is the decoder feature at level l , $W^{(l)} \in \mathbb{R}^{C'_l \times C_l}$ is a 1×1 projection that maps contrast channels C_l to decoder channels C'_l , and $\tilde{F}_c^{(l)}$ denotes the

bilinearly interpolated contrast feature at the spatial resolution of level l . Specifically, the projections adapt: $256 \rightarrow 128$, $128 \rightarrow 64$, $64 \rightarrow 32$, and $32 \rightarrow 32$ at levels $l = 4, 3, 2, 1$ respectively. This multi-scale residual injection enables the refinement network to leverage contrast signals throughout the entire decoding hierarchy, progressively correcting residual misalignment from coarse to fine scales. A final 1×1 convolution produces the registered output $\hat{I}^{(r)} = \mathcal{U}(\hat{I}^{(c)}, \{F_c^{(l)}\})$.

2.6 Loss Function

The training objective combines pixel-wise and perceptual losses applied to both the coarse and final outputs:

$$\mathcal{L} = \mathcal{L}_{\text{final}}(\hat{I}^{(r)}, I_f) + \gamma \cdot \mathcal{L}_{\text{aux}}(\hat{I}^{(c)}, I_f), \quad (3)$$

where $\gamma = 0.3$ weights the auxiliary coarse loss. Each component loss is defined as:

$$\mathcal{L}_{\text{stage}}(P, T) = \|P - T\|_1 + \alpha \|P - T\|_2^2 + \beta(1 - \text{SSIM}(P, T)), \quad (4)$$

with $\alpha = 0.5$ and $\beta = 0.1$. The L1 loss provides robust pixel-wise supervision, the MSE loss penalizes large deviations, and the SSIM loss preserves structural integrity. The auxiliary loss on $\hat{I}^{(c)}$ provides gradient signal to the registration U-Net, encouraging the coarse stage to produce a good initial alignment that facilitates subsequent refinement.

3 Experiments

3.1 Datasets and Implementation Details

Datasets. We evaluate on two benchmarks: (1) **OR-PAM-Reg-4K** [23], comprising 4,248 image pairs at 512×256 resolution from three mice, split into training (3,396), validation (420), and test (432) sets; and (2) **OR-PAM-Reg-Temporal-26K** [24], containing 26,000+ temporally ordered pairs from longitudinal acquisitions, providing a more challenging evaluation with temporal drift and biological variability.

Implementation. The network uses 32 base channels with a $32 \rightarrow 64 \rightarrow 128 \rightarrow 256$ encoder progression (2.56M parameters). Training uses the Adam optimizer ($\text{lr} = 10^{-4}$, weight decay 10^{-5}) with cosine annealing over 100 epochs, batch size 8, and gradient clipping (max norm 1.0). Mixed precision (AMP) is employed for memory efficiency. All experiments use a single NVIDIA GPU with seed 42 for reproducibility.

Evaluation Metrics. Since ground-truth registered images are unavailable for bidirectional OR-PAM data, we adopt a reference-free evaluation strategy. For each frame i , the forward (odd) columns O_i serve as the pseudo ground truth for the registered backward (even) columns \hat{E}_i , and we report standard NCC, SSIM,

and PSNR between O_i and \hat{E}_i to quantify intra-frame alignment quality. For inter-frame temporal consistency, no ground truth exists and standard metrics are not directly applicable. We therefore propose two novel metrics. We first construct full merged frames M_i by interleaving O_i and \hat{E}_i back into a $H \times 2W$ image, restoring the original spatial layout. The **Temporal NCC** (TNCC) is defined as the mean NCC between consecutive merged frames:

$$\text{TNCC} = \frac{1}{N-1} \sum_{i=1}^{N-1} \text{NCC}(M_i, M_{i+1}). \quad (5)$$

The reference ceiling TNCC_{ref} is computed identically from consecutive odd-only frames, representing the natural temporal coherence unaffected by registration. The **Temporal NCC Gap** (TNCG) is then defined as:

$$\text{TNCG} = |\text{TNCC} - \text{TNCC}_{\text{ref}}|, \quad (6)$$

where $\text{TNCG} \approx 0$ indicates that registration preserves natural temporal dynamics without introducing frame-to-frame artifacts. An ideal method should maximize intra-frame alignment while minimizing TNCG.

3.2 Comparison with State-of-the-Art

table 1 presents the quantitative comparison on both benchmarks. The proposed method is compared against four traditional methods (SIFT, Demons, Optical Flow, SyN) and three deep learning methods (VoxelMorph, TransMorph, SAS-Net [10]).

Performance analysis. Traditional registration methods achieve NCC below 0.73 on 4K due to the violation of brightness constancy by scan-direction-dependent domain shift. Among deep learning methods, deformation-based approaches (VoxelMorph, TransMorph) perform comparably to SIFT despite learning spatial transformations, confirming that the domain shift fundamentally limits correspondence estimation in pixel space. SAS-Net, which explicitly addresses domain shift through scene-appearance separation, achieves NCC of 0.961 and PSNR of 32.50 dB on 4K.

PCReg-Net achieves NCC of 0.983, SSIM of 0.982, and PSNR of 46.96 dB on 4K, representing improvements of 0.022 in NCC and 14.46 dB in PSNR over SAS-Net. On the larger-scale 26K dataset, the method achieves NCC = 0.998, SSIM = 0.991, and PSNR = 52.61 dB, surpassing SAS-Net by 12.39 dB in PSNR, confirming robust generalization to extended temporal sequences. Notably, the deformation-based methods (VoxelMorph and TransMorph) degrade substantially on 26K ($\text{NCC} \leq 0.74$). In contrast, SAS-Net maintains strong performance ($\text{NCC} = 0.994$), highlighting the importance of domain-shift handling. The deterministic nature of the framework avoids the feature uncertainty that affects probabilistic models [13], contributing to the consistently low variance across test samples.

fig. 2 presents qualitative comparison on representative test samples.

Table 1. Intra-frame registration quality on OR-PAM-Reg-4K (432 test samples) and OR-PAM-Reg-Temporal-26K (2,714 test samples). NCC, SSIM, and PSNR measure alignment between odd and registered even columns. Best in **bold**, second best underlined.

Method	OR-PAM-Reg-4K			OR-PAM-Reg-Temporal-26K		
	NCC↑	SSIM↑	PSNR↑	NCC↑	SSIM↑	PSNR↑
<i>Traditional Methods</i>						
Unregistered	0.167	0.482	19.46	0.190	0.536	18.90
SIFT [8]	0.723	0.679	24.14	0.752	0.745	24.34
Demons [17]	0.323	0.579	20.35	0.347	0.634	20.12
Optical Flow [7]	0.061	0.455	18.99	0.089	0.516	18.80
SyN [1]	0.411	0.613	21.55	0.505	0.691	21.73
<i>Deep Learning Methods</i>						
VoxelMorph [2]	0.724	0.659	22.88	0.741	0.594	22.84
TransMorph [3]	0.594	0.641	21.09	0.693	0.653	22.07
SAS-Net [10]	0.961	<u>0.894</u>	<u>32.50</u>	<u>0.994</u>	<u>0.972</u>	40.22
PCReg-Net (Ours)	0.983	0.982	46.96	0.998	0.991	52.61

3.3 Temporal Consistency Evaluation

Beyond single-frame alignment quality, we evaluate temporal consistency across consecutive frames—a critical requirement for longitudinal OR-PAM studies. Using the TNCC and TNCG metrics defined in section 3.1, we assess whether each registration method preserves the natural temporal dynamics when registered even columns are merged with odd columns to form full frames.

table 2 presents the temporal evaluation results. Traditional methods that introduce frame-dependent artifacts degrade temporal coherence: SIFT (TNCG = 0.0726), Optical Flow (TNCG = 0.0404), and SyN (TNCG = 0.0401) all exhibit substantial deviation from TNCC_{ref}. Deformation-based deep learning methods similarly produce temporal artifacts: VoxelMorph (TNCG = 0.0702) and TransMorph (TNCG = 0.0538), as their learned deformation fields amplify inter-frame variability. SAS-Net achieves much better temporal consistency (TNCG = 0.0038) with strong intra-frame alignment (NCC = 0.994). PCReg-Net achieves the best intra-frame quality (NCC = 0.998, SSIM = 0.991) while maintaining near-zero temporal consistency gap (TNCG = 0.0001), indicating that the registration preserves the natural temporal dynamics of the underlying tissue without introducing frame-to-frame artifacts.

3.4 Ablation Study

Systematic ablation experiments validate each architectural component. Five configurations are evaluated on OR-PAM-Reg-4K with 50 training epochs and seed 42.

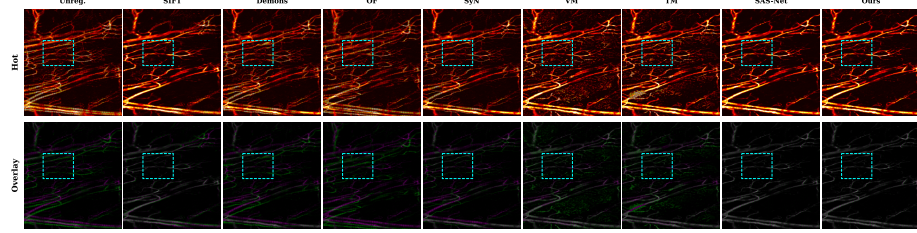


Fig. 2. Qualitative comparison on a representative 26K test sample. **Top row:** merged full frame (odd + registered even interleaved) in *hot* colormap; smooth appearance indicates good alignment. **Bottom row:** magenta/green overlay where odd columns are magenta and registered even columns are green; well-aligned regions appear gray, misaligned regions show colored fringes. Traditional methods (SIFT, Demons, OF, SyN) and deformation-based methods (VM, TM) exhibit visible artifacts, while our method achieves near-perfect alignment with no visible fringes.

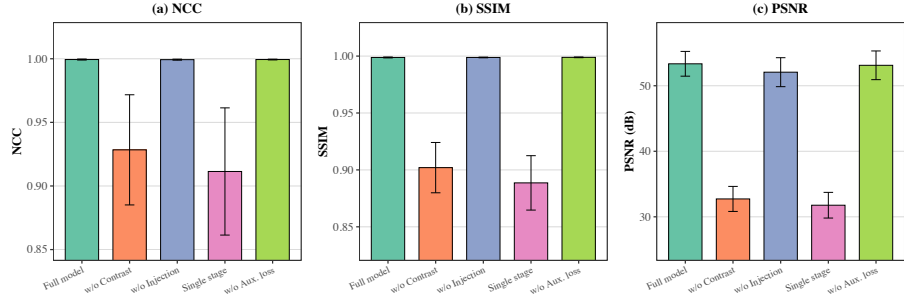


Fig. 3. Ablation study results showing NCC and SSIM across five configurations. The full model achieves the best performance, with each component contributing to the final result.

Effect of contrast module. Removing the contrast module causes a dramatic drop: NCC falls from 0.999 to 0.928 (-7.1%) and PSNR from 53.35 to 32.73 dB (-20.62 dB). This confirms that explicitly comparing coarse-registered and reference features is critical for the refinement network to identify residual misalignment.

Effect of feature injection. Disabling the feature injection layers reduces PSNR from 53.35 to 52.07 dB (-1.28 dB) while NCC remains at 0.999. The multi-scale contrast features injected into the decoder provide complementary guidance that refines sub-pixel alignment, particularly benefiting PSNR.

Single-stage baseline. Using only the Registration U-Net output $\hat{I}^{(c)}$ without refinement yields NCC = 0.911 and PSNR = 31.77 dB, a drop of -21.58 dB from the full model. This demonstrates that the coarse stage alone is insufficient for

Table 2. Temporal consistency evaluation on OR-PAM-Reg-Temporal-26K (2,691 consecutive frame pairs). NCC and SSIM measure single-frame alignment quality. TNCC measures temporal coherence of consecutive full merged frames. TNCG measures deviation from $\text{TNCC}_{\text{ref}} = 0.963$. Best in **bold**, second best underlined.

Method	NCC \uparrow	SSIM \uparrow	TNCC \uparrow	TNCG \downarrow
Odd-only (TNCC_{ref})	—	—	0.963	—
<i>Traditional Methods</i>				
SIFT [8]	0.752	0.745	0.891	0.0726
Demons [17]	0.347	0.634	0.938	0.0259
Optical Flow [7]	0.089	0.516	0.923	0.0404
SyN [1]	0.505	0.691	0.923	0.0401
<i>Deep Learning Methods</i>				
VoxelMorph [2]	0.741	0.594	0.893	0.0702
TransMorph [3]	0.693	0.653	0.910	0.0538
SAS-Net [10]	<u>0.994</u>	<u>0.972</u>	<u>0.967</u>	<u>0.0038</u>
PCReg-Net (Ours)	0.998	0.991	0.964	0.0001

Table 3. Ablation study on OR-PAM-Reg-4K (50 epochs). Each row removes one component from the full model. Best in **bold**.

Configuration	NCC \uparrow	SSIM \uparrow	PSNR (dB) \uparrow
Full model	0.999	0.999	53.35
w/o Contrast module	0.928	0.902	32.73
w/o Feature injection	0.999	0.999	52.07
Single stage only	0.911	0.889	31.77
w/o Auxiliary loss ($\gamma = 0$)	0.999	0.999	53.12

high-fidelity alignment, and the refinement stage provides substantial quality gains.

Effect of auxiliary loss. Setting $\gamma = 0$ slightly reduces PSNR from 53.35 to 53.12 dB (-0.23 dB). While the effect is modest, auxiliary supervision on $\hat{I}^{(c)}$ provides a consistent improvement by encouraging the coarse stage to produce better initial alignment for refinement. This observation aligns with multi-task learning principles [12], where jointly optimizing related objectives yields shared representations that benefit downstream tasks.

4 Conclusion

We present PCReg-Net, a progressive contrast-guided registration framework for bidirectional OR-PAM alignment. By decomposing the registration into coarse alignment followed by contrast-guided refinement, PCReg-Net achieves high-fidelity registration quality (NCC = 0.983, SSIM = 0.982, PSNR = 46.96 dB) on

the OR-PAM-Reg-4K benchmark, surpassing the state-of-the-art by over 14 dB in PSNR. Temporal consistency evaluation on OR-PAM-Reg-Temporal-26K using the proposed TNCC and TNCG metrics demonstrates that PCReg-Net preserves natural inter-frame dynamics with near-zero TNCG from the reference ceiling. The multi-scale contrast module and feature injection mechanism enable explicit identification and correction of residual misalignment at multiple scales. Ablation studies confirm the contribution of each component, and efficiency analysis demonstrates real-time capability. The framework provides a reliable solution for high-speed bidirectional OR-PAM imaging and is applicable to other scanning microscopy modalities with similar alignment challenges.

References

1. Avants, B.B., Epstein, C.L., Grossman, M., Gee, J.C.: Symmetric diffeomorphic image registration with cross-correlation: Evaluating automated labeling of elderly and neurodegenerative brain. *Med. Image Anal.* **12**(1), 26–41 (Feb 2008) [2](#), [7](#), [9](#)
2. Balakrishnan, G., Zhao, A., Sabuncu, M.R., Guttag, J., Dalca, A.V.: VoxelMorph: A learning framework for deformable medical image registration. *IEEE Trans. Med. Imaging* **38**(8), 1788–1800 (Aug 2019) [2](#), [7](#), [9](#)
3. Chen, J., Frey, E.C., He, Y., Segars, W.P., Li, Y., Du, Y.: TransMorph: Transformer for unsupervised medical image registration. *Med. Image Anal.* **82**, 102615 (Nov 2022) [2](#), [7](#), [9](#)
4. Chen, J., Liu, Y., Wei, S., Bian, Z., Subramanian, S., Carass, A., Prince, J.L., Du, Y.: A survey on deep learning in medical image registration: New technologies, uncertainty, evaluation metrics, and beyond. *Med. Image Anal.* **100**, 103385 (Feb 2025) [2](#)
5. Cho, S., Kim, M., Ahn, J., Kim, Y., Lim, J., Park, J., Kim, H.H., Kim, W.J., Kim, C.: An ultrasensitive and broadband transparent ultrasound transducer for ultrasound and photoacoustic imaging in-vivo. *Nat. Commun.* **15**(1), 1444 (Feb 2024) [1](#)
6. Cikaluk, B.D., Restall, B.S., Haven, N.J.M., Martell, M.T., McAlister, E.A., Zemp, R.J.: Rapid ultraviolet photoacoustic remote sensing microscopy using voice-coil stage scanning. *Opt. Express* **31**(6), 10136–10149 (Mar 2023) [1](#)
7. Horn, B.K., Schunck, B.G.: Determining optical flow. *Artif. Intell.* **17**(1-3), 185–203 (Aug 1981) [2](#), [7](#), [9](#)
8. Lowe, D.G.: Distinctive image features from scale-invariant keypoints. *Int. J. Comput. Vis.* **60**(2), 91–110 (Nov 2004) [2](#), [7](#), [9](#)
9. Maraghechi, S., Hoefnagels, J.P.M., Peerlings, R.H.J., Geers, M.G.D.: Correction of scan line shift artifacts in scanning electron microscopy: An extended digital image correlation framework. *Ultramicroscopy* **187**, 144–163 (Apr 2018) [1](#)
10. Qin, J.: SAS-Net: Scene-appearance separation network for robust spatiotemporal registration in bidirectional photoacoustic microscopy. *arXiv preprint* (2026) [2](#), [6](#), [7](#), [9](#)
11. Qin, J., Liu, F., Zong, L.: BC-PMJRS: A brain computing-inspired predefined multimodal joint representation spaces for enhanced cross-modal learning. *Neural Networks* **188**, 107449 (Apr 2025) [2](#)
12. Qin, J., Liu, K., Cai, Y., Ji, T., Liu, F.: MTLP-MDG: Multi-task learning framework using probabilistic distribution perception for missing data generation. In:

2025 International Joint Conference on Neural Networks (IJCNN). pp. 1–8 (2025) 9

13. Qin, J., Peng, B., Liu, F., Cheng, G., Zong, L.: DUAL: Dynamic uncertainty-aware learning. arXiv preprint arXiv:2506.03158 (2025) 6
14. Qin, J., Wang, Y.: Learning domain-invariant representations for cross-domain image registration via scene-appearance disentanglement. arXiv preprint arXiv:2601.08875 (2026) 2
15. Qin, J., Xu, Y., Lu, Z., Zhang, X.: Alternative telescopic displacement: An efficient multimodal alignment method. arXiv preprint arXiv:2306.16950 (2023) 2
16. Shintate, R., Ishii, T., Ahn, J., Kim, J.Y., Kim, C., Saijo, Y.: High-speed optical resolution photoacoustic microscopy with MEMS scanner using a novel and simple distortion correction method. *Sci. Rep.* **12**(1), 9221 (June 2022) 1
17. Vercauteren, T., Pennec, X., Perchant, A., Ayache, N.: Diffeomorphic demons: Efficient non-parametric image registration. *NeuroImage* **45**(1), S61–S72 (Mar 2009) 2, 7, 9
18. Wang, L.V., Hu, S.: Photoacoustic tomography: In vivo imaging from organelles to organs. *Science* **335**(6075), 1458–1462 (Mar 2012) 1
19. Yang, F., Wang, Z., Shi, W., Wang, M., Ma, R., Zhang, W., Li, X., Wang, E., Xie, W., Zhang, Z., Shen, Q., Zhou, F., Yang, S.: Advancing insights into in vivo meningeal lymphatic vessels with stereoscopic wide-field photoacoustic microscopy. *Light Sci. Appl.* **13**(1), 96 (Apr 2024) 1
20. Yao, J., Wang, L., Yang, J.M., Maslov, K.I., Wong, T.T.W., Li, L., Huang, C.H., Zou, J., Wang, L.V.: High-speed label-free functional photoacoustic microscopy of mouse brain in action. *Nat. Methods* **12**(5), 407–410 (May 2015) 1
21. Yao, J., Wang, L.V.: Photoacoustic microscopy. *Laser Photon. Rev.* **7**(5), 758–778 (2013) 1
22. Zhang, H.F., Maslov, K., Stoica, G., Wang, L.V.: Functional photoacoustic microscopy for high-resolution and noninvasive in vivo imaging. *Nat. Biotechnol.* **24**(7), 848–851 (July 2006) 1
23. Zhang, T., Yan, C., Lan, X.: OR-PAM-Reg-4K: A benchmark dataset for bidirectional OR-PAM registration (2026) 5
24. Zhang, T., Yan, C., Lan, X.: OR-PAM-Reg-Temporal-26K: A large-scale longitudinal benchmark for bidirectional OR-PAM registration (2026) 5